Direct measurement of steady fluid forces upon a deformed cylinder in confined axial flow

Aurélien Joly[a,b,*], Nicolas de Buretel de Chassey[a], Alexandre Martin[b], Olivier Cadot[c], Luc Pastur[d,b], Pierre Moussou[a,b]

[a] *EDF Lab Paris-Saclay, 7 bd Gaspard Monge, 91120 Palaiseau, France*
[b] *IMSIA UMR CNRS-EDF-CEA-ENSTA 9219*
[c] *School of Engineering, The University of Liverpool, Liverpool L69 3BX, UK*
[d] *ENSTA Paris, 828 bd des Maréchaux, 91120 Palaiseau, France*

Abstract

This paper addresses the case of a cylinder array in axial flow at Reynolds numbers from 60 000 to 110 000. A comprehensive experimental and numerical study of the steady fluid forces arising from a geometrical perturbation in the array arrangement is carried out and compared with a semi-empirical model from the literature. The test rig consists of a 3x3 confined cylinder bundle with a pitch-to-diameter ratio equal to 1.33. The central cylinder can be rotated, translated or bent. Global forces and moments as well as pressure profiles at several sections are measured. Velocity profiles at both sides of the cylinder are also collected. Additionally, RANS simulations (Reynolds-averaged Navier–Stokes) are carried out. Pressure loss effects similar to the ones occurring in hydraulic pipes are found to play a major role on the velocity field. Rotation tests are in agreement with the literature: at low angles of incidence, the lift force is proportional to the angle. The supporting rod at the centre of the cylinder strongly disturbs the local lift force but does not change the global linear trend. In translation, the wake of the support generates a fluid stiffness effect. Bending tests allow to assess all terms of the semi-empirical model from the literature, which proves to be quite accurate at a sufficient distance from the ends and from the supports. In addition, the investigation provides refined quantitative measurements of local and global force coefficients of the statically deformed cylinder in rotation, translation and bending.

Keywords: cylinder array, axial flow, pressure measurement, CFD, semi-empirical model

© 2021. This manuscript version is made available under the CC-BY-NC-ND 4.0 license
http://creativecommons.org/licenses/by-nc-nd/4.0/
DOI of published paper: https://doi.org/10.1016/j.jfluidstructs.2021.103326

1. Introduction

Fluid-structure interaction plays a major role in the dynamic behaviour of industrial structures such as fuel assemblies in nuclear cores (see e.g. Moussou et al., 2017; Ricciardi, 2018). An example of such a structure consists of a 4 m high and 20 cm wide bundle of 17x17 fuel rods tied together by means of spacer grids. In order to extract the heat produced by the nuclear fuel, the

*Corresponding author

assemblies are submitted to an axial flow of water, from bottom to top. The industrial issue can be simplified by considering the fuel assembly as a slender and relatively flexible structure in axial flow. Being able to describe the fluid forces exerted upon fuel assemblies requires understanding those upon the simplest slender structure: the cylinder.

The contemporary model of fluid forces upon a flexible cylinder in axial flow is based on theoretical works conducted in the 1950s and 1960s. Taylor (1952) distinguished several roughness types of the cylinder surface and gave in each case an expression of the local fluid forces upon a cylinder section depending only on the local angle of incidence. These expressions were given in terms of normal and tangential force relatively to the deformed cylinder axis. According to Taylor's own words, they were 'entirely speculative', since the only experimental data available at that time gave the force upon a straight cylinder inclined by steps of 10° (Relf and Powell, 1917). Lighthill (1960a) chose a different approach and derived a theoretical expression of the inviscid fluid force in the framework of the slender body approximation. This assumption greatly simplified the potential flow calculation: in the case of a uniform cross-section, it reduces to the 2-D problem of an oscillating body in quiescent fluid, thus giving rise to an added mass force. For a statically deformed cylinder, the local fluid force depends only on the local curvature of the cylinder. Hawthorne (1961) combined both approaches. From Taylor (1952), he selected the roughness case of 'a number of long projections pointing equally in all directions'. The linearized expression given in this case assumes that, at low angles of incidence, the force acting upon a cylinder section reduces to the friction drag (parallel to the incident flow) due to these protuberances. This leads to a constant tangential force and a normal force proportional to the local angle of incidence. From Lighthill (1960b), Hawthorne selected the simplified expression proposed for a body with a uniform cross-section. He then simply added up both terms, Lighthill's inviscid force and Taylor's viscous force, and established the first equation of motion of a flexible cylinder in axial flow. Later, Païdoussis (1966a) used and developed this model, that is denoted from now on the Taylor-Lighthill-Païdoussis (TLP) model. He explored the stability of the equation of motion for different boundary conditions (pinned-pinned, clamped-clamped, clamped-free). He also undertook experiments with a single cylinder in a water tunnel in low confinement conditions (Païdoussis, 1966b). Good agreement was reported between theory and experimental results with respect to the critical flow velocities at the onset of instabilities (buckling or flutter), but the model failed to predict accurately the frequency of oscillation in the case of flutter. The model being linear, it could neither predict the amplitude of flutter oscillations nor the maximum displacement in buckling.

As a first step of improvement of the model, Païdoussis (1973) gave a version taking into account confinement effects. He related the longitudinal force upon the cylinder to the pressure losses in the channel, and introduced a confinement-dependent added mass coefficient. That version can be used for a flexible cylinder in a cluster of cylinders, provided that the other cylinders are rigid. Taking into account the coupling between several flexible cylinders is itself a whole branch of the research in the field of axial flows (see e.g. Chen, 1975a,b; Chung and Chen, 1977; Païdoussis and Suss, 1977; Païdoussis, 1979; Adjiman et al., 2016; De Ridder et al., 2017). Another branch of the research was focused on deriving non-linear versions of the equations of motion, in order to enhance the predictions as compared to the linear version. Further details can be found in the comprehensive three-part paper Païdoussis et al. (2002), Lopes et al. (2002) and Semler et al. (2002) in the case of a clamped-free cylinder, and Modarres-Sadeghi et al. (2005) in the pinned-pinned configuration. These works and further ones are reviewed in Païdoussis (2016).

Until relatively recently, the force model consisting of Lighthill's inviscid term and Taylor's

viscous term had been assessed essentially by its ability to predict the onset of instability. The coefficients of the model were fitted to dynamical tests in the framework of the quasi-steady assumption. No comparison with direct force measurements had been carried out. This lack of validation data began to be overcome thanks to the study of Ersdal and Faltinsen (2006). They conducted experiments with a long straight cylinder in a towing tank and measured the normal force at low angles of incidence. The value obtained for the normal force coefficient was substantially higher than usual values recommended in the literature. This led the authors to state that the normal force could not be explained by skin friction alone, thus questioning Taylor's assumption. High values of the normal force coefficient derived from forced oscillations experiments had already been reported much earlier (Chen and Wambsganss, 1972), but the direct measurements by Ersdal and Faltinsen (2006) made this clear. Divaret et al. (2014) performed similar experiments with a straight cylinder in a wind tunnel. Yet they first looked at their results in terms of lift and drag instead of normal and tangential force. They noticed that the lift force (transverse to the incident flow) was proportional to the angle of incidence, thus not behaving as in Taylor's assumption of zero lift at low angles of incidence. In addition, they observed that the contribution of lift in the normal force dominated the contribution of drag, and that by a factor of about 10. Pressure measurements along the cylinder surface helped to explain the linear behaviour of the lift force, thus confirming that this force did not merely originate from friction. De Ridder et al. (2015) carried out numerical simulations with a straight cylinder in axial flow. Their results were in agreement with the findings of Divaret et al. (2014), and they identified a dependency of the lift coefficient to the inlet turbulence intensity. See table 1 for a review of the results on the lift coefficient in the recent literature. De Ridder et al. (2015) also investigated the case of a curved cylinder and found that the decomposition into an inviscid term and a viscous term was accurate at low curvatures. To the best of the authors' knowledge, no other reference in the literature compares the actual fluid forces and the ones predicted by the TLP model in the case of a curved cylinder.

In the industrial application that motivated the present study, fuel assemblies stand beside each other, with narrow gaps between them. Therefore, the case of a confined cylinder needs be taken into account. To the authors' knowledge, no direct measurement of the steady lift and of the drag coefficients in the case of a slightly inclined cylinder is available in the literature in confined conditions. Moreover, confinement raises the question of a possible translatory fluid stiffness: does any lift force appear when the cylinder moves close to a facing wall? Furthermore, the issue of the validity of the TLP model for a curved cylinder, whether confined or not, deserves also some further attention.

To address these goals, a combined experimental and numerical approach is undertaken. A specific confinement geometry is chosen, namely a deformable cylinder inside a rigid cylinder array. The array properties (pattern and pitch-to-diameter ratio) are chosen in order to match the ones in the industrial structure. Velocity measurements in the experiment are supported by velocity field analyses in the computational fluid dynamics (CFD) model. They provide further insight into the flow pattern details. Global and local force measurements are carried out and compared to numerical results. § 2 gives all relevant details on the experimental setup and the numerical model. The results are exposed in § 3. They are discussed with respect to the TLP model in § 4.

	Ersdal and Faltinsen (2006)	Divaret et al. (2014)	De Ridder et al. (2015)		
geometry	unconfined	unconfined	confined in circular channel, $D_{ch} \simeq 10D$		
L/D	31	60	28		
test facility	towing tank	wind tunnel	CFD		
angle range	±4°	±6°	0 – 1°		
angle steps	1°	2°	0.1°		
Re_D	27 000–45 000	24 000	16 000		
inlet turbulence intensity	n/a	< 0.3 %	0.1 %	10 %	10 %[a]
c_L [rd^{-1}]	0.06	0.10 ± 0.01	0.01	0.07	0.11

[a]The inlet turbulence length scale is set higher in this case than in the previous one.

Table 1: Experimental and numerical studies from the literature about the lift coefficient of a slightly inclined cylinder in axial flow. c_L is the absolute value of the slope between the angle of incidence and the lift coefficient.

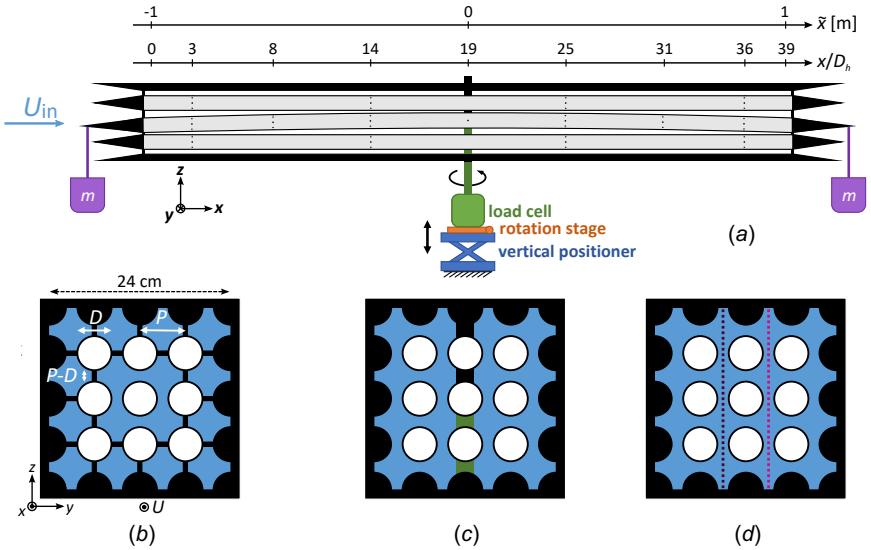

Figure 1: Experimental setup: (*a*) side view, (*b*) front view at entrance section ($x = 0$), (*c*) front view at middle section ($\tilde{x} = 0$), and (*d*) front view at $x/D_h = 36$ or any other similar section (the dotted lines represent the measurement positions of the velocity profiles).

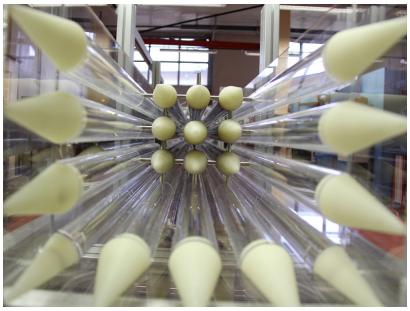

(*a*)

(*b*)

Figure 2: Photographs of the test rig: (*a*) front view (here without upper wall) and (*b*) side view.

2. Experimental and numerical procedure

2.1. A wind tunnel test rig

2.1.1. Fixed part of the geometry

The scheme of the experimental model is shown in figure 1 with some photographs in figure 2. It consists of a square bundle of 3x3 cylinders (figure 1a, b) with pitch-to-diameter ratio $P/D = 1.33$ (as defined in figure 1b), length $L = 2\,\mathrm{m}$ and width 24 cm, set up in a wind tunnel. The x-axis indicates the main flow direction, y and z are the transverse directions. The x-coordinate starts at the beginning of the cylinders (excluding the tapered ends), as illustrated in figure 1(a). For convenience, the coordinate $\tilde{x} = x - L/2$ is also introduced, so that $\tilde{x} = 0$ at the cylinder centre. Both coordinates x and $\tilde{x}$ are used throughout the paper.

The walls of the test section are equipped with half cylinders, such that the developing boundary layers at the wall mimic the ones of a larger number of surrounding cylinders. For the bundle, thin-walled aluminium cylinders of diameter $D = 4.5\,\mathrm{cm}$ and thickness 2 mm are chosen, in order to minimise static deflection under their own weight. Their bending stiffness is high enough to avoid their deformation during the wind tunnel tests. The eight neighbour cylinders are supported at both ends via a grid of cylindrical elements of diameter 0.8 cm as shown in figure 1(b) and observable in the photograph in figure 2(a).

2.1.2. Mobile part of the geometry

The central cylinder is supported at its centre only, so as to enable its rotation and translation. The supporting rod has a diameter of $D_r = 2.2\,\mathrm{cm}$, it is displayed in green in figures 1(a, c) and figure 3. In order to have a symmetric geometry, a similar rod is added on the top of the cylinder, removable and without support function.

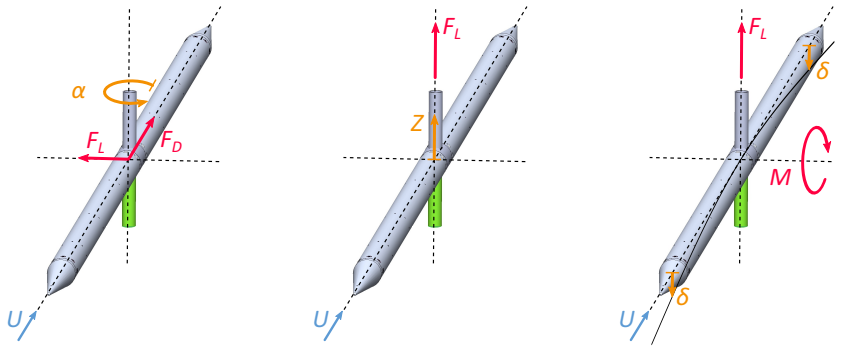

Figure 3: Degrees of freedom of the central cylinder, tunable parameters and relevant fluid forces: (*a*) rotation, (*b*) translation and (*c*) bending. The green part of the vertical support is always present, its grey part is removable in order to characterize its effect on the aerodynamic loading of the cylinder.

The angle of incidence α of the cylinder is set by a rotation stage (Newport M-UTR160), the stiffness of which being high enough to prevent noticeable deflections at the cylinder ends due to vibration. The vernier on the side of the rotation stage allows to read the angle with 5 arcmin = 0.08° resolution. The angle is varied in a range of ±30 arcmin = ±0.5°.

For the translatory displacement Z, a vertical positioner (Newport 281) is used. The position is set with the help of a ruler of resolution 1 mm mounted on the side of the positioner. The range of Z is ±10 mm.

Bending is achieved by loading the central cylinder at both ends, as depicted in figure 1(*a*). The deflection δ at the cylinder ends is obtained from standard beam theory:

$$\delta = \frac{mgL^3}{24EI}\left(1 + 3\frac{l}{L}\right), \tag{1}$$

where m is the load mass on each end, g is the gravity acceleration, $E = 62$ GPa is the elastic modulus of aluminium, $I = 6.26 \times 10^{-8}$ m^4 is the moment of inertia of the cylinder cross section, and $l = 16$ cm is the distance between the end of the cylinder and the point of application of the load on the tapered end. The deformed shape $w(\tilde{x})$ in z-direction reads:

$$w(\tilde{x}) = -\frac{2\delta}{(1 + 3l/L)L^3}\left(3(1 + 2l/L)L\tilde{x}^2 - 2\,|\tilde{x}|^3\right). \tag{2}$$

Loading at both ends is carried out by steps of 0.6 kg, generating a deflection of 0.63 mm. The full load is 6 kg at each end, reaching a theoretical deflection of 6.3 mm. The overall calibration of the procedure is achieved by comparing the deflection with the maximal weight to its theoretical value by tuning the displacement Z so that the cylinder ends are in contact with the lower cylinder.

In this paper, rotation (α), translation (Z) and bending (δ) are called the three degrees of freedom of the central cylinder.

2.1.3. Force measurements

The steady fluid forces exerted upon the central cylinder are measured using an AMTI MC3A-100 6-axis load cell. Time signals are recorded at a sample rate of 1 kHz and averaged

over 30 s. Precision tests performed with standard weights indicate an accuracy of ±20 mN of the load cell in vertical direction (z). The measurement range of the load cell and thus its accuracy is four times narrower in horizontal direction (x, y), hence reaching ±5 mN. Careful handle of thermal drift and precise control of test conditions, such as room temperature, allow for even more accurate measurements.

Drag, lift and pitching moment are studied depending on the three degrees of freedom of the central cylinder as shown in figure 3. The drag F_D is the force in the main flow direction (x). The lift F_L is the transverse force in the plane of displacement or deformation of the cylinder. Hence, it corresponds to the force in y-direction for rotation and in z-direction for translation and bending (figures 1 and 3). The pitching moment M is evaluated at the cylinder centre (figure 3c).

In the following, the fluid forces are presented in terms of force coefficients according to standard definitions:

$$C_L = \frac{F_L}{\frac{1}{2}\rho U^2 DL} \quad \text{and} \quad C_D = \frac{F_D}{\frac{1}{2}\rho U^2 DL}, \tag{3}$$

where C_L is the lift coefficient, C_D is the drag coefficient, ρ is the fluid density and U is the average velocity in the channel. The moment coefficient is defined as:

$$C_M = \frac{M}{\frac{1}{2}\rho U^2 DL^2}. \tag{4}$$

The superscript 0 denotes the force coefficient measured in the neutral configuration ($\alpha = 0, Z = 0, \delta = 0$). Symmetries imply that all lateral forces are zero, $C_L^0 = 0$. Experimentally, small asymmetries offset the values of the lift and moment. Since the ranges of the parameters are narrow (see § 2.1.2), these offsets are of the same order of magnitude as the ranges of the fluid forces. For instance, $C_L^0 = 1.7 \times 10^{-3}$ at Re = 66 000 while for $\alpha \neq 0$ it varies from 0.5×10^{-3} to 2.8×10^{-3} for $\alpha \in [-0.5^\circ\ ;\ 0.5^\circ]$. To allow for comparison with the CFD results, which do comply with the symmetries, experimental curves are translated so that they fit together at the neutral configuration. The variation about the neutral configuration is $\widetilde{C_L} = C_L - C_L^0$. In the following, any quantity $\widetilde{X}$ denotes the variation of X about the neutral configuration.

The influence of the supporting rod of the central cylinder on the fluid forces is unknown. In the previous section, it was mentioned that the geometry has been made symmetric by adding a rod on the top of the cylinder. In order to assess the influence of the support, measurements are carried out both with and without the removable upper rod; the corresponding curves are given here only when it leads to noticeably different results.

2.1.4. Velocity measurements

The incoming velocity upstream of the cylinders U_{in} (figure 1a) is measured by means of a Pitot tube (KIMO, type L) placed at the centre of the entrance section and connected to a manometer (KIMO C310-H0). The turbulent intensity of the incoming flow is 0.7 %. Its spatial inhomogeneity is 1.5 % (standard deviation).

The mean velocity in the test section U is calculated by multiplying the upstream velocity by the area ratio between the entrance square section $(4P)^2$ and the flow section between the cylinders $(4P)^2 - 16\pi(D/2)^2$ (see figure 1b): $U = 1.79 U_{\text{in}}$. The Reynolds number is based on the hydraulic diameter $D_h = D\left(4(P/D)^2 - \pi\right)/(P/D + \pi - 1) = 5.14$ cm. In the experiment, U can reach up to 32 m/s, which gives a maximum Reynolds number of $UD_h/\nu_{\text{air}} \simeq 110\,000$. It is about four times smaller than the Reynolds number in a reactor core (Re $\simeq$ 400 000).

Velocity profiles along the vertical axis at both sides of the central cylinder (figure 1*d*) and in different sections along the model (x-axis) are measured by means of thin Pitot-like tubes (diameter 1.6 mm), using a Scanivalve DSA 3217/16Px pressure scanner at a sample rate of 100 Hz and averaging over 10 s at each measurement point. These two tubes (one at each side of the central cylinder) measure the total pressure, while the static pressure is recorded from pressure taps at the surface of the cylinders. The estimated accuracy of the corresponding measurement is about 2 %.

2.1.5. Pressure measurements

To gain access to the fluid force distribution in the experiment, local force measurement upon the central cylinder is also arranged. It requires the design of a specific cylinder with a large number of pressure taps. This cylinder consists of six instrumented aluminium rings assembled with pieces of plain aluminium tube, resulting in measurement sections at x/D_h = 3, 8, 14, 25, 31 and 36, as drawn in figure 1. Each of these rings is equipped with 16 pressure holes of diameter 0.5 mm, which gives an azimuthal resolution of 22.5°. Vinyl tubes of inner diameter 1 mm and length ranging between 35 cm and 2.15 m are used to make the link between the pressure taps and the measurement devices. Because of this design, loading the cylinder at its ends and determining accurately its deflection is not possible. Therefore, pressure measurement results are available only for rotation and translation of the cylinder.

All pressure taps of the first section ($x/D_h = 3$) as well as one pressure tap out of two of the second ($x/D_h = 8$) and third ($x/D_h = 14$) sections are connected to a miniature pressure scanner installed inside the cylinder (Scanivalve ZOC22b, range $\pm 5\,''\mathrm{H_2O}$, 32 channels). The remaining 64 pressure taps are connected to two pressure scanners outside the wind tunnel (Scanivalve DSA 3217/16Px, range $\pm 5\,''\mathrm{H_2O}$, 16 channels each). They are measured alternately in groups of 32. Time signals are recorded at a sample rate of 50 Hz and averaged over 30 s. To reach the best achievable precision, an in-situ calibration of the pressure scanners is performed before the measurements using a pressure calibrator (Furness Controls FCO560, range ±2000 Pa, itself calibrated 16 months before the measurement campaign). The zero of the scanners is reset before each test. The drift in warm conditions is of about 2 Pa/h, thus being negligible during a 30 s acquisition. Therefore, unlike measurements with the load cell, pressure measurements do not require drift compensation.

In order to obtain a non-dimensional pressure coefficient C_p at each measurement point, a reference pressure p_{ref} must be defined, so that $C_p = (p - p_{\mathrm{ref}})/\left(1/2\rho U^2\right)$. Because of pressure losses along the model, the reference pressure is chosen to be section-dependent. Hence the use of the following definition:

$$C_p(x,\theta) = \frac{p(x,\theta) - \bar{p}(x)}{\frac{1}{2}\rho U^2}, \tag{5}$$

where $\bar{p}$ is the average over the 16 pressure taps of the section and θ is the azimuthal angle (figure 4).

The physical quantity measured by the scanners is the difference between the pressure in each vinyl tube and a common reference pressure. Here, the reference channel is set at atmospheric pressure. The pressure in each vinyl tube is assumed to be equal to the pressure at the cylinder wall if there were no hole. Geometrical imperfections of pressure holes lead to systematic errors on C_p of about 1 % (Tavoularis, 2005). In the narrow range of geometrical variation that is studied here (e.g. $\alpha = \pm 0.5°$), this may have a significant impact on the pressure profiles. Therefore, the results are presented in terms of differential value of C_p with regards to the neutral configuration

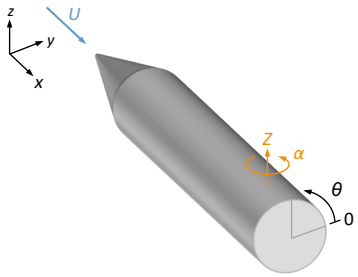

Figure 4: Orientation of the azimuthal angle θ in pressure measurements.

($\alpha = 0, Z = 0, \delta = 0$):

$$\widetilde{C}_p(\theta) = C_p(\theta) - C_p^0(\theta), \tag{6}$$

and this at each measurement section (x). Another processing step is carried out before looking into the results: since a linear behaviour is expected for the rotational degree of freedom (Divaret et al., 2014), the pressure profiles are shown relatively to the angle of incidence. Thus, the curves $\widetilde{C}_p(\theta)/\alpha$ are displayed. For translation, a similar treatment is applied: the curves $\widetilde{C}_p(\theta)/(Z/(P-D))$ are shown. The non-dimensional displacement $Z/(P-D)$ is 0 when the cylinder is in neutral configuration and ± 1 when there is contact with a neighbour cylinder. Eventually, since this is the goal of the pressure measurements, the integrated local fluid force is shown:

$$\widetilde{C}_N(\alpha) = -\frac{1}{2}\int_0^{2\pi} \widetilde{C}_p(\theta)\cos\theta d\theta, \tag{7}$$

where C_N denotes the normal force coefficient in rotation. For translation, the vertical lift coefficient is calculated as:

$$\widetilde{C}_L(Z) = -\frac{1}{2}\int_0^{2\pi} \widetilde{C}_p(\theta)\sin\theta d\theta. \tag{8}$$

In early tests, tripping of the boundary layer was found to have an influence on the pressure profiles. Tripping is achieved by means of 26 mm-wide adhesive rough strips stuck onto all nine cylinders ($x/D_h \in [0.6\ ;\ 1.1]$). For rotation, results are shown both with and without tripping. For translation, pressure measurements are only shown with tripping. When not explicitly mentioned, force measurements using the load cell as well as velocity measurements are performed *without* tripping.

2.2. RANS simulations

The numerical results presented here were obtained via RANS simulations (Reynolds-averaged Navier–Stokes) performed with Code_Saturne 4.0, an EDF in-house open CFD tool based on a collocated finite volume approach (Archambeau et al., 2004). The code uses a centred scheme for the velocity and a SIMPLEC algorithm (semi-implicit method for pressure linked equations – consistent) for the velocity-pressure coupling. For turbulence modelling, the $k-\omega$ SST (shear stress transport) model with a two-scale wall law is used. This was previously found to be well-suited to the prediction of the fluid force upon a single cylinder in near-axial flow (Divaret et al., 2014). The $k-\omega$ SST model was also used in the past in several other studies on fluid forces

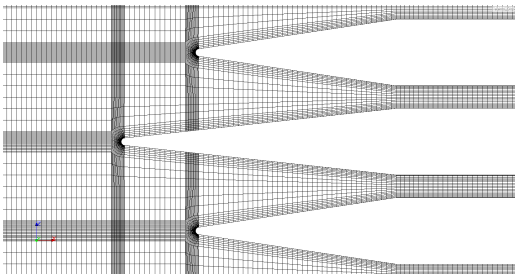

(*a*)

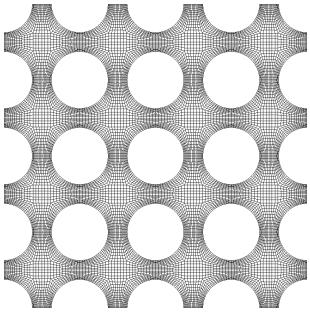

(*b*)

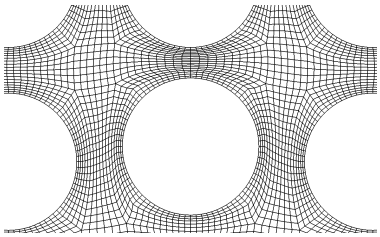

(*c*)

Figure 5: Section views of the mesh: (*a*) side view at $y = 0$, (*b*) front view for $x/D_h \in [0\ ;\ 39]$, and (*c*) detailed front view in a translation case ($Z = 5\,\text{mm}$).

upon slender structures in axial flow (Adjiman et al., 2016; De Ridder et al., 2013, 2015, 2017; De Santis and Shams, 2017; ter Hofstede et al., 2017; Papukchiev et al., 2018).

The fluid volume is discretized with a conform hexahedral mesh generated using the software SALOME 7.8.0. The geometry of the numerical model is almost identical to the one of the experiment, the only difference is that all cross-flow elements supporting the cylinders as shown in figure 1(b, c) are not included. The resulting mesh is made up of 12.3 million cells, see figure 5(a, b). It is refined close to the walls. Cell sizes are adjusted according to best practice guidelines for these types of flow and turbulence model. The non-dimensional cell half-thickness, commonly denoted by y^+, should thus remain between 20 and 40. Because of the geometrical specificities of the present mesh, y^+ actually lies between 12 and 41, which is an acceptable compromise. The mesh is generated in the neutral configuration. To deform the mesh according to the three degrees of freedom previously described (figure 3), a solid mechanics computation is performed on the fluid domain with Code_Aster 14.1 with an imposed displacement on the central cylinder. The cells at the wall are ensured to keep their previously prescribed size by imposing the displacement on several mesh layers around the cylinders as illustrated in figure 5(c).

The time step was chosen such that the Courant–Friedrichs–Lewy condition CFL < 1 is met everywhere, where CFL is the Courant number. 1.0 s of physical time is simulated with a total of 200 000 time steps. The maximum *CFL* is found at the cylinder tips and its value is 0.52. A constant and uniform velocity $U_{\text{in}} = 10\,\text{m/s}$ is imposed at the inlet (Re = 61 000) and a constant static pressure at the outlet. The sides of the domain and the cylinder walls are modelled as smooth walls.

The global fluid forces and moments are computed at each time step and then averaged over the last 0.1 s of the simulation, when the steady flow has clearly established. Flow visualizations are produced with ParaView at the last time step.

Other numerical simulations were performed with a coarser mesh, in neutral configuration. Changing the cell length in streamwise direction Δx from 3.33 mm (reference) to 5 mm led to a reduction by 1 % of the drag coefficient C_D. Another time step was also tested, for the simulations with a rotated cylinder: increasing Δt from 0.5×10^{-5} s to 2.0×10^{-5} s led to a reduction of the Taylor-Divaret coefficient c_L by 1.7 %. Only the results obtained in the reference case are presented in this paper.

3. Results

This section provides the experimental and numerical results that were produced with the geometry described in the previous section. Some insights into the velocity fields and pressure losses in the neutral configuration are first presented. The subsequent paragraphs then detail the results separately for each degree of freedom.

3.1. Flow characterisation in neutral configuration

Figure 6 shows profiles of the axial velocity u measured at six different cross-sections over the vertical positions displayed in figure 1(d). The two downward peaks observed at $x/D_h = 3$ and $x/D_h = 8$ are the momentum deficiencies in the wakes of the supporting cylindrical elements shown in figure 1(b). They diffuse and eventually disappear downstream. Boundary layers at the cylinders' walls develop and merge after some 25 hydraulic diameters, leading to a quasi-homogeneous flow in the axial direction. This recalls the concept of entrance length in a pipe.

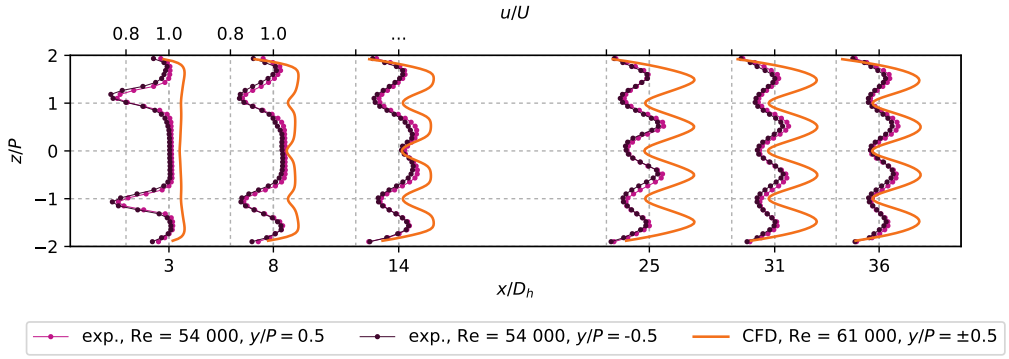

Figure 6: Axial velocity u, profiles at both sides of the cylinder and different cross-sections along the model. Experimental and numerical results.

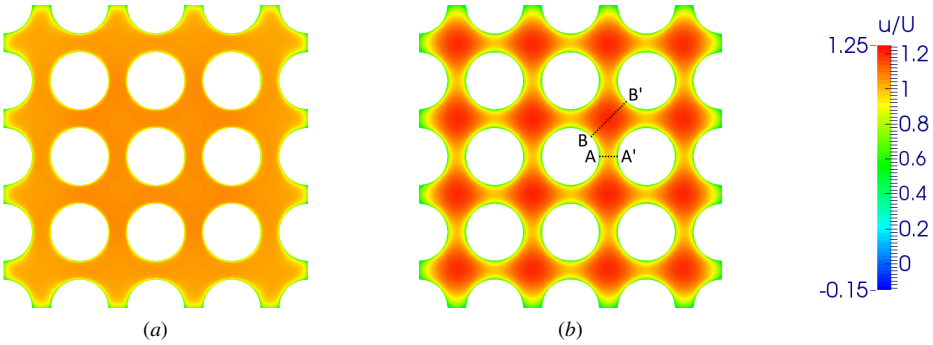

Figure 7: Axial velocity fields from CFD: (a) at the entrance of the bundle, $x = 0$, and (b) downstream where the flow is homogeneous in the axial direction, $x/D_h = 35$. Re = 61 000.

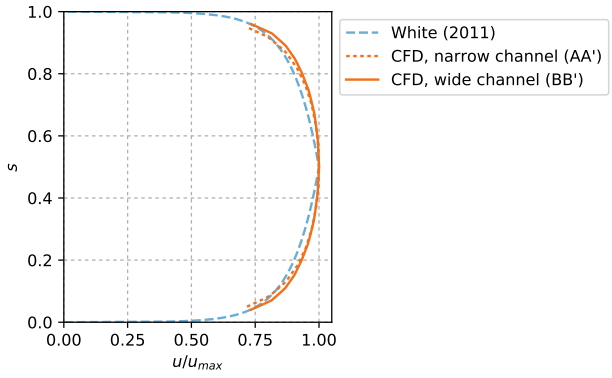

Figure 8: Axial velocity profiles from CFD along the two paths at $x/D_h = 35$ (AA' and BB') displayed in figure 7(b), s is the non-dimensional coordinate along the path. Re = 61 000.

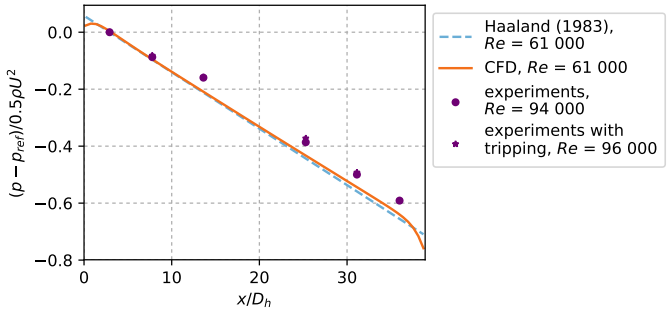

Figure 9: Non-dimensional pressure losses along the model. CFD values are taken from a line parallel to the x-axis at the centre of a wide channel ($y/P = z/P = 0.5$). Each experimental point is obtained by averaging the values of the 16 pressure taps at the corresponding section. The reference pressure is chosen to be the one at the first section ($x/D_h = 2.9$).

Using the expression $L_e/d = 1.6\mathrm{Re}^{1/4}$ (White, 2011) and replacing d by D_h yields $L_e = 24D_h$ in the conditions of the experiment (Re = 54 000), which is consistent with the measurements.

The developed boundary layers lead to lower velocities in narrow regions of the cross section and higher velocities in wide areas. The amplitude of the velocity oscillations is smaller in the experiments than in CFD. This is likely to be produced by the additional turbulent mixing associated with all the cross-flow elements. Also, the global flow rate is remarkably larger in CFD. This indicates thinner boundary layers in the experiment, which is, as well, likely to be explained by the additional mixing.

The numerical simulations can provide more detailed information on the velocity variations within a cross-section. Figure 7 gives two examples of velocity fields at different positions along the cylinder bundle. Figure 8 shows the non-dimensional velocity profiles between two cylinder walls in the narrowest channel (AA') as well as in the widest one (BB'), in the established-flow zone ($x/D_h > 24$). The velocity close to the wall is not given, since the solver applies a wall law in the first cell of the mesh at the cylinder wall. The numerical profiles are compared with a standard log profile of the turbulent flow in a pipe (White, 2011) at the same Reynolds number as in the simulations. A good agreement is found between these profiles, which confirms that the flow in the present geometry can be understood by classical turbulent pipe flow considerations, where friction losses dominate.

Figure 9 depicts the resulting pressure losses in CFD and experiments. They are compared with an empirical law by Haaland (1983) that gives the linear pressure loss coefficient in a pipe, λ_c, as a function of the Reynolds number only (based on the hydraulic diameter):

$$\frac{1}{\sqrt{\lambda_c}} = -1.8 \log_{10}\left(\frac{6.9}{\mathrm{Re}_{D_h}}\right). \tag{9}$$

The dashed line of figure 9 is then obtained through the definition of the linear pressure loss coefficient:

$$\frac{p - p_{\mathrm{ref}}}{1/2\rho U^2} = \frac{x - x_{\mathrm{ref}}}{D_h}\lambda_c. \tag{10}$$

There is a very good overall agreement between all the results presented in figure 9. The pressure losses in the simulations are very regularly distributed except for the regions close to the cylinder ends. Experimental pressure losses are less perfectly linear. This is likely to be produced by the

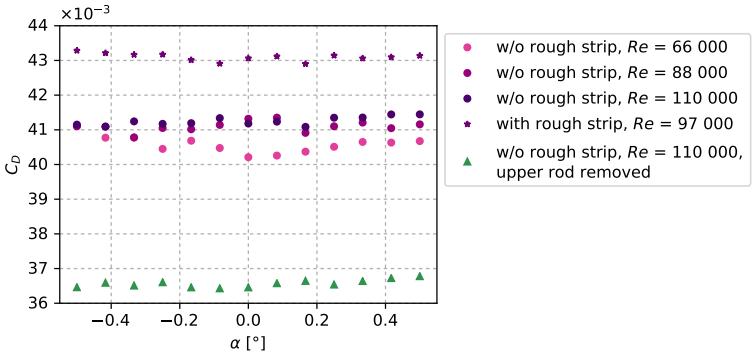

Figure 10: Cylinder in rotation: drag coefficient of a slightly inclined cylinder in axial flow, experimental results.

source	tripping	supporting rod	tapered ends	Re	$C_D \times 10^3$
experiments	no	upper and lower part	included	110 000	41.3
experiments	no	lower part only	included	110 000	36.6
experiments	no	no support	included		31.9
experiments	yes	upper and lower part	included	97 000	43.1
experiments	yes	no support	included		33.7
CFD	yes	no support	included	61 000	33.3
CFD	yes	no support	excluded	61 000	15.8
TLP: Haaland (1983)		n/a (friction drag)	n/a	61 000	15.6

Table 2: Drag coefficient of a cylinder in axial flow: comparison between experimental and numerical results. The experimental drag without support is calculated from the measured values with and without the upper part of the supporting rod. Tripping in CFD is included in the turbulence model.

geometrical inhomogeneities of the test rig in the streamwise direction. The use of a tripping rough strip does not seem to have a significant influence (the circles and the stars can hardly be distinguished).

3.2. Rotation

3.2.1. Global forces

Figure 10 shows the experimental drag measurements of the central cylinder with small inclinations. The variations of the drag as a function of the angle of incidence do not display any clear trend. In the experiments without tripping, $C_D = (41.0 \pm 0.7) \times 10^{-3}$ over the range of Reynolds number considered (here the error is simply computed as twice the standard deviation). Tripping the boundary layer does not change this statement; the presence of the rough strip manifests itself in a slight drag increase: $C_D = (43.1 \pm 0.2) \times 10^{-3}$ (5 % increase). This observation is consistent with theory, since a turbulent boundary layer has steeper velocity gradients than a laminar one, thus leading to stronger wall shear stress.

Further values of the drag coefficient in different configurations are given in table 2. Removing the upper part of the supporting rod in the experimental model leads to a reduced drag of

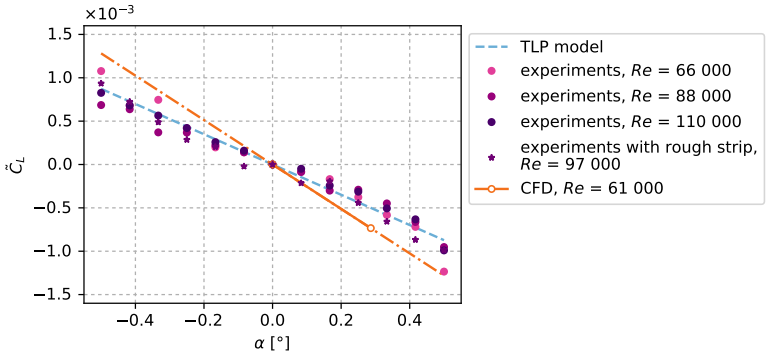

Figure 11: Cylinder in rotation: lift coefficient of a slightly inclined cylinder in axial flow. Filled symbols: experimental results; empty symbols: numerical results. Dashed line: TLP model (see discussion in § 4).

$C_D = 36.6 \times 10^{-3}$ (also shown in figure 10, green triangles). Since there is no support in the simulations, the expected CFD drag should be yet again smaller, by the same difference, hence the predicted value of $C_D = 31.9 \times 10^{-3}$ in table 2. There is no rough strip in the computations, but the turbulence model does simulate a turbulent boundary layer. Therefore, to better compare CFD and experimental results, one last corrective step is applied: the difference between drag with and without rough strip is added to the latter value. This eventually leads to the following calculated support-free drag coefficient from the experiments: $C_D = 33.7 \times 10^{-3}$. The computed drag coefficient from CFD is $C_D = 33.3 \times 10^{-3}$ at Re $= 61\,000$, which is very close to the prediction.

In CFD, the contribution of the tapered ends of the cylinder can be ignored in order to obtain the friction drag along the cylinder, which reduces to $C_D = 15.8 \times 10^{-3}$. The comparison with the TLP model, for drag in rotation as well as for further results, is addressed in the discussion.

Figure 11 shows the lift force upon the cylinder in near-axial flow. All four experimental curves display a linear relationship between the lift and the angle of incidence, which is consistent with the recent literature (Divaret et al., 2014; De Ridder et al., 2015). The absolute value of the slope between the angle of incidence and the lift coefficient is called the Taylor-Divaret coefficient and denoted by c_L (a capital C is used for actual force coefficients and a small c for slopes). It is deduced from the curves by means of a least squares fit and shown in table 3, the uncertainty being determined statistically from the quality of the linear regression. There is no clear influence of the Reynolds number in the explored range. This low sensitivity to Re was also found for the other degrees of freedom. For clarity, only the results at highest Reynolds number will be shown in the following for translation and bending. Tripping the boundary layer with a rough strip does not have an influence on the value of c_L either. The numerical simulations exhibit a similar behaviour as the experiments, however with a slightly higher value of c_L (0.15 vs. about 0.10).

When comparing with existing references (table 1), it appears that the present experimental values of c_L are fairly similar to the one from Divaret et al. (2014), despite the different confinement conditions, Reynolds numbers and angle ranges. The Taylor-Divaret coefficient retrieved from Ersdal and Faltinsen (2006) is slightly smaller (0.06), but the order of magnitude is the same. The numerical results of De Ridder et al. (2015), which are obtained from the central part

geometry	confined in square array of cylinders, $P/D = 1.33$				
L/D	44				
test facility	wind tunnel				CFD
angle range	$\pm 0.5°$				$0 - 0.3°$
angle steps	$0.08°$				$0.3°$
Re_{D_h}	66 000	88 000	97 000[a]	110 000	61 000
inlet turbulence intensity	0.7 %				8 %
c_L [rd^{-1}]	0.11	0.09	0.10	0.10	0.15
uncertainty	± 0.02	± 0.01	± 0.01	± 0.01	n/a

[a] With tripping rough strip.

Table 3: Values of the Taylor-Divaret coefficient c_L in the present experiments and simulations. See table 1 for comparison with the literature.

of the cylinder only (integration over approximately half the length of the cylinder), exhibit a strong sensitivity to the inlet turbulence conditions.

3.2.2. Velocity, pressure and local force distribution

The drag force distribution along the cylinder, which is obtained from CFD and shown in figure 12(*a*), displays an almost uniform behaviour, except in the vicinity of the cylinder ends: for $2\tilde{x}/L \in [-0.75\ ;\ 0.75]$, the local drag coefficient does not deviate from its average by more than 3 %. The force distribution is only plotted along the cylindrical part of the cylinder. The contribution of the tapered ends is estimated by subtracting the integral of the curve in figure 12(*a*) to the total drag as given in table 2. This way, the tapered ends are estimated to account for slightly more than half of the total drag of the central cylinder. The drag upon the tapered ends is likely to be mainly a pressure drag, while the drag upon the cylindrical part is essentially a shear drag.

Figure 12(*b*) displays the spatial distribution of the lift force along the cylinder as obtained from CFD. The force per unit length f retrieved from the numerical results is made non-dimensional so that the curve gives a direct representation of the local value of c_L. It can be seen that this coefficient has strong variations close to the cylinder ends and varies relatively slowly between the values 0.11 and 0.16 in the central part of the cylinder. This trend agrees qualitatively with the observations of De Ridder et al. (2015), who noted a slight increase in c_L from the upstream half of the cylinder to the downstream half.

Axial velocity fields and pressure fields from numerical simulations are shown in figure 13, for the section at $x/D_h = 29$. At this section, the velocity field looks very similar to that of the neutral configuration in figure 7, while the pressure field is polarized, leading to the Taylor-Divaret lift.

Figure 14 (left) shows experimental results on the differential pressure coefficients relatively to the angle of incidence $\widetilde{C}_p/\alpha$, as defined in § 2.1.5, in both cases of tripping of the boundary layer or not. Tripping has a dramatic organizing effect on the first upstream measurement sections ($x/D_h = 3$, 8 and 14), while it is not significant to the downstream half of the cylinder. Laminar

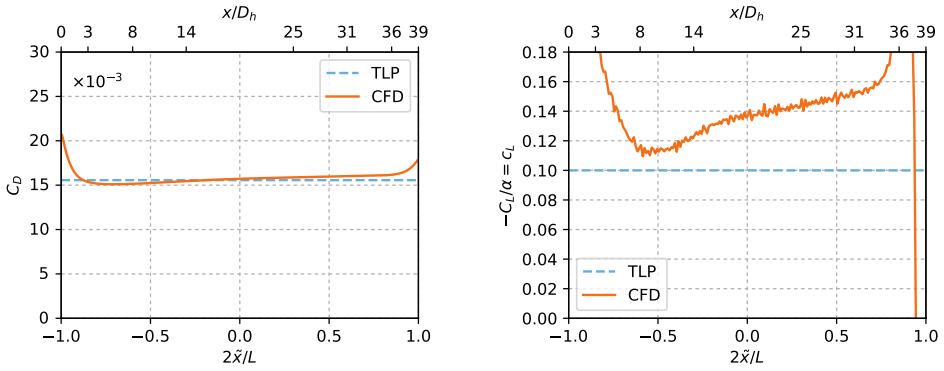

(*a*) (*b*)

Figure 12: Cylinder in rotation: (*a*) drag and (*b*) lift force distribution along the cylinder, simulation at $\alpha = 0.29°$ and Re = 61 000. The local lift force is given in terms of slope relatively to the angle of incidence (Taylor-Divaret coefficient c_L).

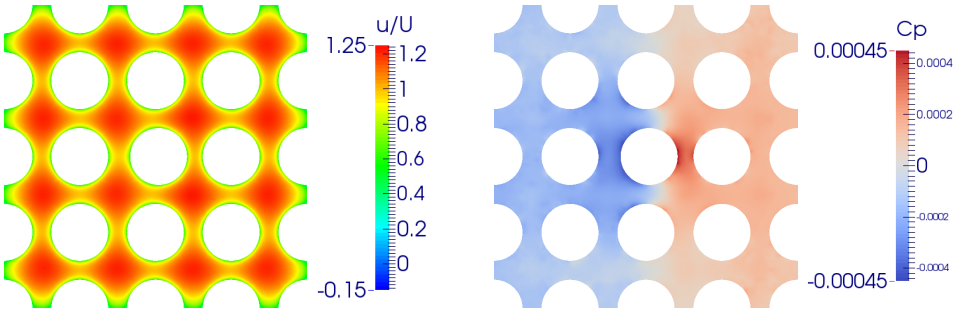

(*a*) (*b*)

Figure 13: Cylinder in rotation: CFD results for $\alpha = 0.29°$ and Re = 61 000 in a cross-section at $x/D_h = 29$, (*a*) axial velocity field and (*b*) pressure coefficient: $C_p(x, y, z) = (p(x, y, z) - \bar{p}(x))/\left(1/2\rho U^2\right)$.

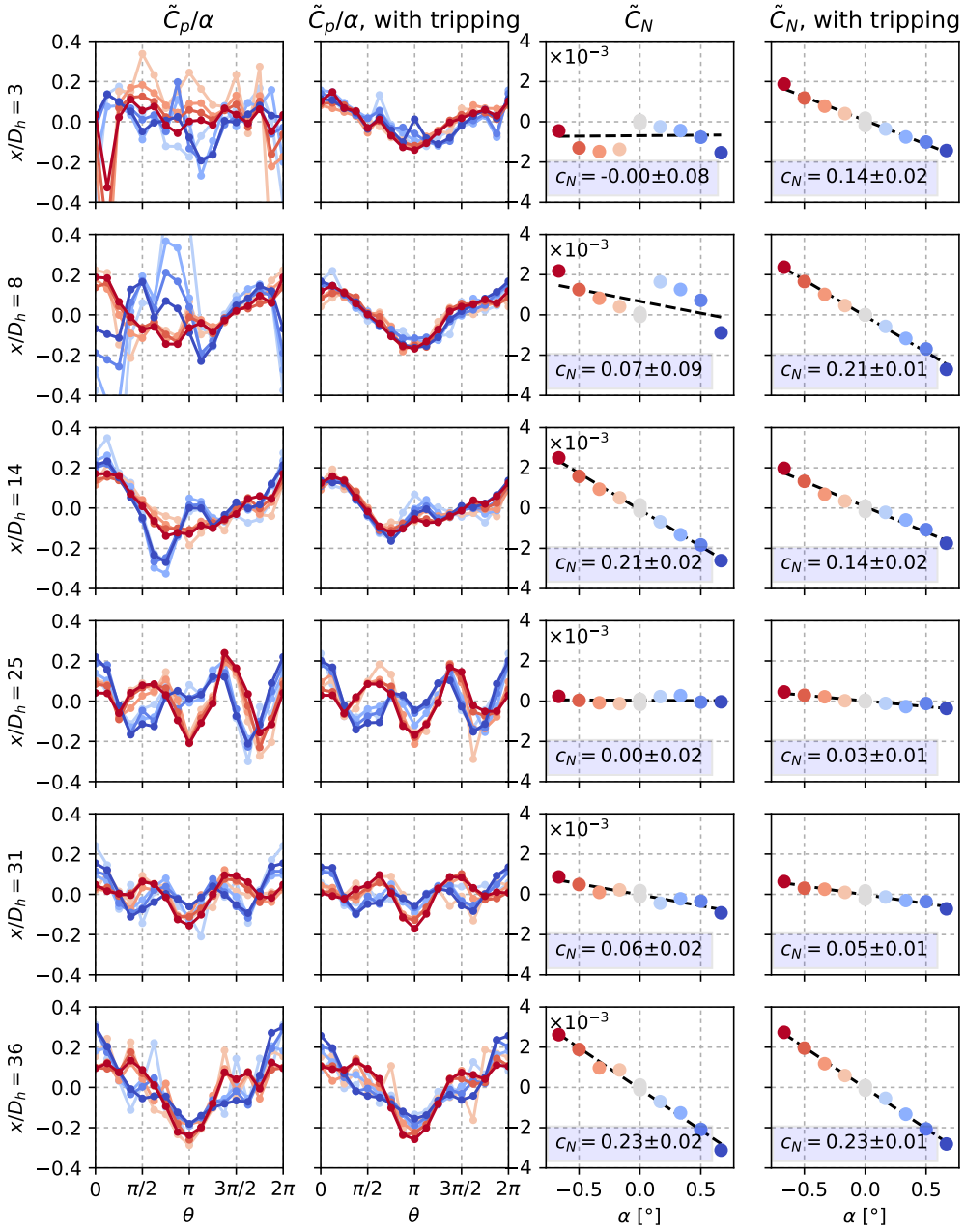

Figure 14: Cylinder in rotation, pressure measurements at different positions along the cylinder, with and without tripping: relative pressure coefficient $\widetilde{C}_p/\alpha$ (left) and integrated normal force coefficient $\widetilde{C}_N$ (right). Re = 96 000. The colour of each curve $\widetilde{C}_p/\alpha$ (left) is chosen according to the value of α. The colour scale is given in the right part of the figure ($\widetilde{C}_N$ curves).

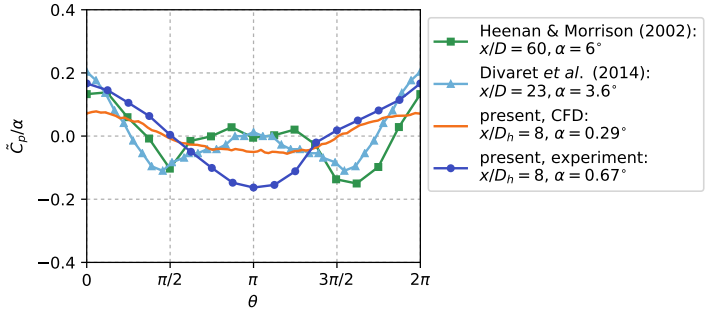

Figure 15: Cylinder in rotation: relative pressure coefficient $\widetilde{C}_p/\alpha$, comparison with CFD and literature references.

to turbulent boundary layer transition triggered by the pressure holes are thus suspected to occur on the cylinders in the first part of the bundle without tripping. Further comments focus on the profiles with tripping. The three sections of the upstream part as well as the last section display pressure profiles with essentially a mode 1 shape as expected by the symmetry breaking produced by the cylinder rotation $\alpha \neq 0$. As observed in CFD in figure 13(b), it corresponds to a higher pressure upon the side facing the flow ($\theta = 0$ when $\alpha > 0$) and a lower pressure upon the opposite side ($\theta = \pi$). The section at $x/D_h = 14$ displays a slight asymmetry but does comply with the main idea of that statement. The central supporting rod (shown in figure 1b) is responsible for the mode 2 shape observed in the profiles at $x/D_h = 25$ and 31, with two maxima at about $\pi/2$ and $3\pi/2$ consistent with the wakes produced by its upper and lower part. The relative pressure profiles $\widetilde{C}_p/\alpha$ overlap very well for all values of α in the upstream half of the cylinder, except for some specific measurement points. Thus, the linear behaviour previously observed from global force measurements is also to be seen in local pressure measurements. In the downstream half of the cylinder, there is a relatively clear distinction between the profiles for $\alpha < 0$ (red colour) and those for $\alpha > 0$ (blue colour). This asymmetric behaviour after the supporting rod is retrieved in additional measurements at several Reynolds numbers, but with slight variations of the profiles. This could be related to the complex reattachment of the flow separated from the supporting rod onto the central cylinder.

Figure 14 (right) shows the resulting local normal force coefficient $\widetilde{C}_N$ (7) at each measurement section. As previously observed, tripping has a great organizing influence on the two upstream sections. On the other sections, the results are relatively similar whether the boundary layer is tripped or not. Now focusing on the results with tripping, a similar behaviour is observed in the upstream half of the cylinder and in the downstream-most section: the normal force is a linear function of the angle of incidence, with c_N ranging from 0.14 to 0.23. In the two sections downstream of the central supporting rod, the linear regression yields much lower slopes: $c_N \in [0.03\ ;\ 0.05]$. The weighted average slope over the cylinder is $c_N = 0.12$. The Taylor-Divaret coefficient is then retrieved from $c_L = c_N/\cos\alpha - C_D \tan\alpha/\alpha \simeq c_N - C_D$, where the value of the friction drag C_D is taken from the numerical simulations (table 2). The result is $c_L = 0.11$, which is consistent with the force measurements of § 3.2.1 (see table 3).

Figure 15 compares one of the present pressure profiles with examples from the literature (Divaret et al., 2014; Heenan and Morrison, 2002) and with the present CFD results. The geometrical configuration in those two references is unconfined. Also, the angles of incidence are much higher ($\alpha = 3.6°$ and 6°), leading to the characteristic shape of the pressure profile on a

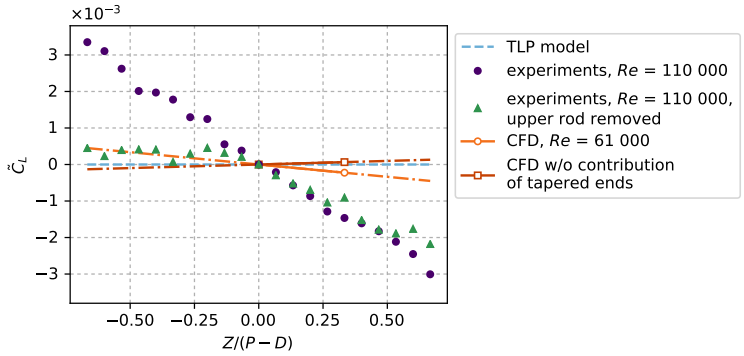

Figure 16: Cylinder in translation: comparison of lift coefficients obtained in the experiments, the numerical simulations and the TLP model (see discussion in § 4).

cylinder with separated flow: two symmetric minima (here at $\pi/2$ and $3\pi/2$) and a higher plateau between them. In the present case, with very low angles of incidence ($\alpha < 0.7°$), the shape is simpler, going from the maximum at $\theta = 0$ to the minimum at $\theta = \pi$. The values of the maximum and minimum are coherent between all experimental data. The CFD profile is a bit flatter, although it displays the same shape as in the present measurements.

3.3. Translation

Drag measurements for a translated cylinder are very similar to those obtained in rotation. They are not shown here, but are available in Joly (2018, p. 58).

3.3.1. Global forces: lift

Figure 16 shows the lift as a function of the non-dimensional displacement $Z/(P - D)$. In the tests where both sides of the supporting rod are present (as illustrated in figure 3), the results display a positive fluid stiffness effect (purple circles in figure 16*b*): the force is a linear function of the displacement and it is opposed to it. The non-dimensional stiffness is defined as:

$$c_k = -\frac{\widetilde{C}_L}{Z/(P-D)}. \tag{11}$$

A linear fit gives $c_k = (4.6 \pm 0.2) \times 10^{-3}$. At the maximal displacement, the lift coefficient $\widetilde{C}_L$ grossly reaches 3×10^{-3}. This is about three times the maximal value of the lift coefficient in rotation (figure 11). Thus, the positive fluid stiffness is not negligible.

However, removing the upper rod (green triangles) considerably reduces the stiffness for $Z < 0$. In CFD (empty circles), the fluid stiffness is hardly noticeable. It completely disappears when the contribution of the tapered ends is excluded (squares). Accordingly, it can be concluded that the positive fluid stiffness observed in the experiments is caused by the wake confinement of the vertical support.

3.3.2. Velocity, pressure and local force distribution

Figure 17 shows the lift force distribution along the cylinder translated by $Z/(P - D) = 0.33$ computed with the numerical simulations, where no supporting part is modelled. Except for

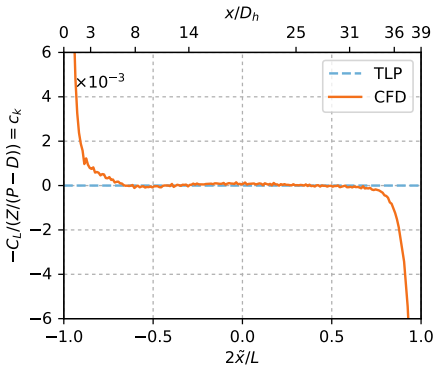

Figure 17: Cylinder in translation: lift force distribution along the cylinder, simulation at $Z/(P-D) = 0.33$ and Re = 61 000.

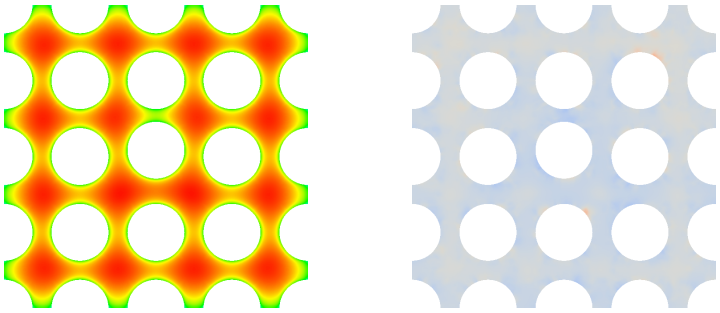

(*a*) (*b*)

Figure 18: Cylinder in translation: CFD results for $Z/(P-D) = 0.33$ and Re = 61 000 in a cross-section at $x/D_h = 29$, (*a*) axial velocity field and (*b*) pressure coefficient C_p. The coulour scales are the same as in figure 13.

the regions close to the cylinder ends, the force upon the cylinder sections is negligible. This confirms that the fluid stiffness identified in the experiments is induced by the support.

Similarly to what has been done in the rotational degree of freedom, figure 18 shows axial velocity and pressure fields from numerical simulations, for the section at $x/D_h = 29$ and in the case of a translated cylinder. Experimental velocity profiles are also available in that case, see figure 19. It appears that bringing the cylinder closer to one of its neighbours reduces the velocity in the narrowed region between them. This happens without any noticeable impact on the pressure, which remains uniform, as expected from the results on the fluid forces.

Figure 20 shows the results of the pressure measurements for translation, in terms of relative differential pressure coefficients $\widetilde{C}_p/(Z/(P-D))$ (6) and local lift coefficient $\widetilde{C}_L$ (8). Only the results where the boundary layer is tripped are shown. The pressure profiles are relatively flat in the upstream part. In the downstream part, they show a sine-like shape with maximum at $\theta = \pi/2$. This pattern is the most pronounced at the section directly downstream of the central support. This translates into a strong fluid stiffness trend on this portion of the cylinder. On the upstream sections, the fluid stiffness is rather slightly negative, but not significant. The weighted average gives $c_k = 1.7 \times 10^{-3}$, which is lower by a factor 3 than what was measured with the load

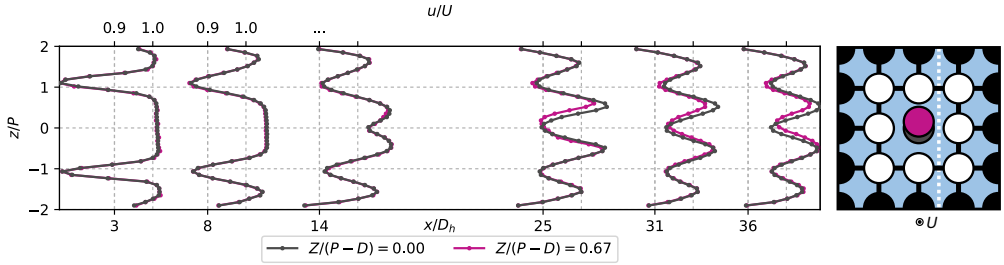

Figure 19: Axial velocity profiles for a translated cylinder. Experimental results, Re = 54 000.

cell ($c_k = 4.6 \times 10^{-3}$). The local fluid stiffness might thus be even stronger directly downstream of the support (the measurement section lies 6 hydraulic diameters downstream of it). This tends to confirm the confinement effect produced from above and below by the neighbour cylinders on the wake of the supporting rod.

3.4. Bending

3.4.1. Global lift and moment

Figure 21(*a*) presents the global lift of a bent cylinder as a function of the non-dimensional deflection $2\delta/L$. This parameter is given in degrees, since it can be understood as an angle; doing this allows for comparison with the results in rotation (e.g. with figure 11). The experiments as well as the numerical simulations show a slight negative trend of the lift with increasing deflection. Removing the contribution of the tapered ends yields the opposite behaviour. This emphasizes that the local fluid forces at the cylinder ends can have a non-negligible influence on the global force. As for the moment (figure 21*b*), experiments and simulations agree well with each other. Here, the contribution of the tapered ends does not make a significant difference.

3.4.2. Local lift force distribution

Figure 22 presents the lift force distribution along the cylinder from CFD. Away from the regions close to the cylinder ends, the following trend is observed: relatively steady increase of the lift force in the upstream half, slope discontinuity in the middle and a much flatter evolution in the downstream half.

4. Discussion

The Taylor-Lighthill-Païdoussis model of fluid forces upon a flexible cylinder in axial and confined flow was already mentioned in the introduction. For each force investigated in the previous section, the expression of the force is now given according to this model in the specific case of a statically deformed cylinder, and compared with the results. The version of the model that is examined here is inspired by Païdoussis (1973) and includes the results of Divaret et al. (2014) about the non-zero viscous lift force.

4.1. Drag

The TLP model assumes a constant and uniform local drag:

$$f_D^{\mathrm{TLP}} = \frac{1}{2}\rho U^2 D C_D. \tag{12}$$

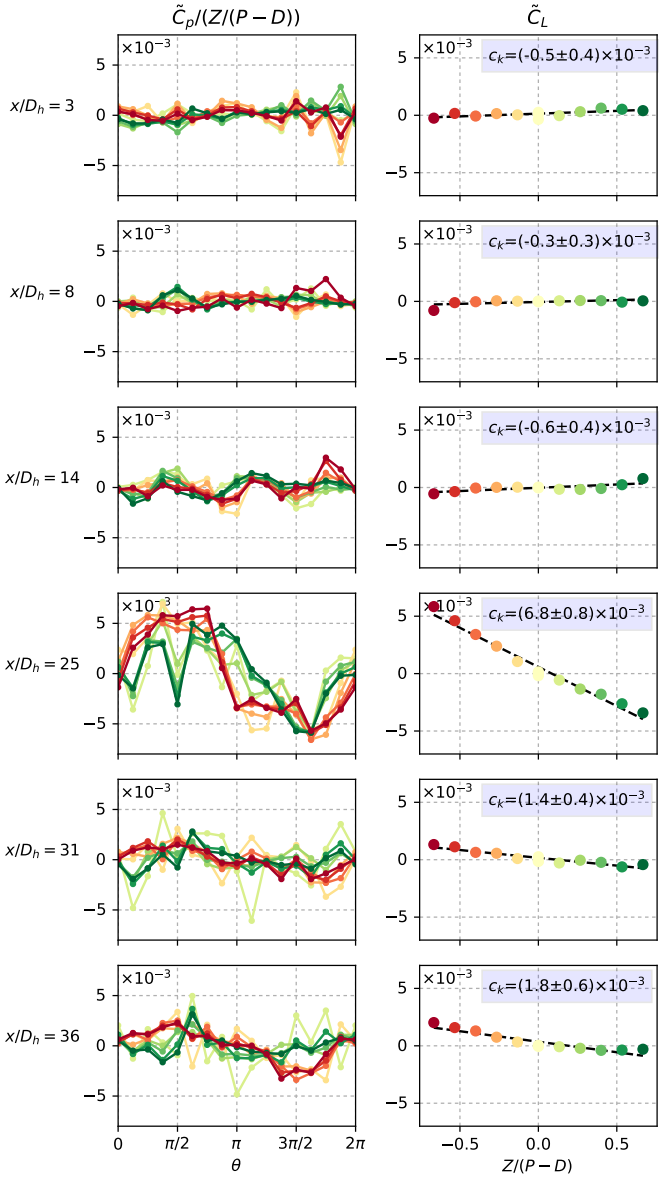

Figure 20: Cylinder in translation: relative pressure coefficient $\widetilde{C}_p/(Z/(P-D))$ and integrated lift force coefficient $\widetilde{C}_L$, with tripping. Re = 98 000. The colour of each curve $\widetilde{C}_p/(Z/(P-D))$ (left) is chosen according to the value of Z. The colour scale is given in the right part of the figure ($\widetilde{C}_L$ curves).

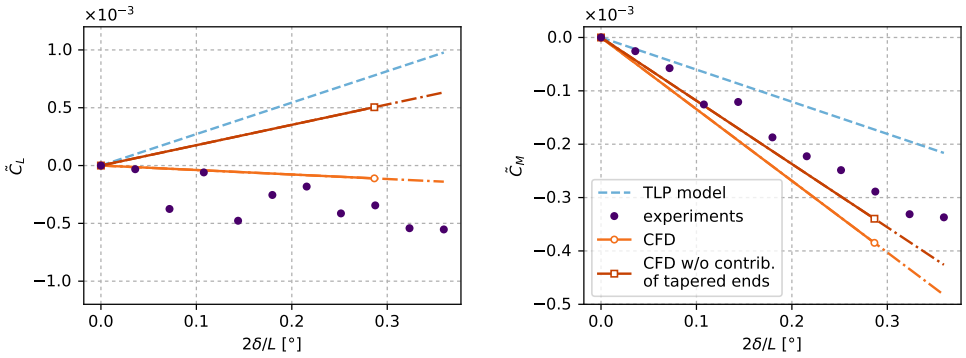

(*a*) (*b*)

Figure 21: Cylinder in bending: (*a*) lift coefficient and (*b*) non-dimensional pitching moment. Filled symbols: experimental results (Re = 110 000); empty symbols: numerical results (Re = 61 000). Dashed line: TLP model (see discussion in § 4).

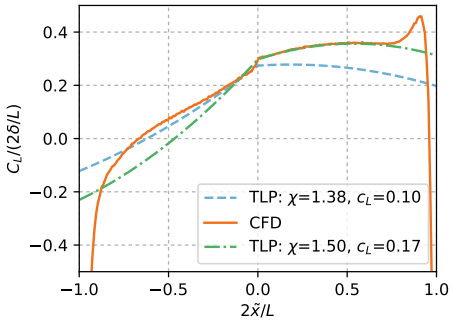

Figure 22: Cylinder in bending: lift force distribution along the cylinder, simulation at $2\delta/L = 0.29°$. Two sets of coefficients are shown for the TLP model (see discussion in § 4).

In the confined case, Païdoussis (1973) suggests to calculate the friction drag from the pressure losses by writing the equilibrium between friction forces and pressure forces in the channel:

$$C_D = \frac{\pi}{4}\lambda_c. \tag{13}$$

The pressure loss coefficient λ_c can in turn be estimated from empirical pressure loss formula, such as those given in Haaland (1983). Using (9) with Re = 61 000 (value used in CFD simulations) yields $C_D = 15.6 \times 10^{-3}$.

In the measurements, the drag is indeed found to undergo negligible variations when slightly perturbing the geometry of the cylinder bundle (§ 3.2.1, figure 10 for rotation). Retrieving the friction drag coefficient from CFD leads to a value which is very close to the one predicted from pressure losses (15.8×10^{-3} vs. 15.6×10^{-3}, see table 2), and this despite the entrance length phenomenon mentioned in § 3.1. Moreover, when considering portions of the cylinder that are not close to the cylinder ends, the drag is found to abide relatively well by the uniform behaviour predicted in the TLP model (figure 12*a*). Also, the good agreement found on the drag value between the experiments and the simulations indicates that the wakes of the cross-flow elements do not substantially influence the global friction drag. The ends of the cylinders do have a non-negligible contribution to the total drag (slightly over 50 %, as deduced from table 2). This is usually taken into account when using the TLP model for instability predictions. Expressions of the forces at the ends can be found e.g. in de Langre et al. (2007) for the tip of a clamped–free cylinder, or in Rinaldi and Païdoussis (2020) for the head of a free–clamped cylinder.

4.2. Lift

In the TLP model, the local lift force is expanded into two terms: an inviscid term (Lighthill), proportional to the local curvature and to the added mass, and a viscous term (Taylor-Divaret), proportional to the local angle:

$$f_L^{\mathrm{TLP}} = -\chi\rho S\, U^2 w'' - \frac{1}{2}\rho U^2 D c_L w', \tag{14}$$

where χ is the added mass coefficient and S is the cylinder cross-section. The superscript $'$ denotes the spatial derivative, so that w' is the local angle and w'' is the local curvature. The added mass coefficient can be evaluated from tests in quiescent fluid or 2–D potential flow calculations. Moretti and Lowery (1976) performed tests in quiescent water with an unconfined bundle of 3x3 cylinders where the central cylinder was excited and the forces were measured. For the pitch-to-diameter ratio 1.33, they obtained $\chi = 1.38$. Despite the increased confinement in the present case, that value is used for comparison with the results. The Taylor-Divaret coefficient c_L can be measured via experiments with a long and straight cylinder slightly inclined in axial flow. As a reference for comparison, the value of Divaret et al. (2014) with an unconfined cylinder is taken: $c_L = 0.10$.

Rotation

For a rotated cylinder with angle of incidence α, there is no curvature and the local lift force reduces to the following uniform expression:

$$f_L^{\mathrm{TLP}} = -\frac{1}{2}\rho U^2 D c_L \alpha. \tag{15}$$

The global lift force is then:

$$F_L^{\mathrm{TLP}} = -\frac{1}{2}\rho U^2 D L c_L \alpha, \tag{16}$$

where the contribution of the cylinder ends has been ignored.

For the global lift force, the expected linear relationship with the angle of incidence appears very clearly in the results (§ 3.2.1, figure 11). The slope taken from Divaret et al. (2014) is very similar to the ones obtained experimentally in the present study (table 3), despite several differences of setup. In particular, the confinement does not seem to have a significant effect on the value of the Taylor-Divaret coefficient c_L.

For the local lift force, the assumption of a uniform distribution is not completely valid, as can be seen from the CFD results (figure 12*b*) for a geometry without supports. The experimental investigation of the normal force distribution by means of pressure measurements (figure 14) shows that a real geometry including supports will lead to even stronger inhomogeneities, especially in the wake of the supports. Yet the linear relationship between the local normal force and the angle of incidence persists at all measurement cross sections, which on the whole induces a linear behaviour of the global force. Untripped ends generate highly uneven pressure profiles in the upstream sections, which does not significantly affect the overall lift measurement. Tripping the boundary layer has a dramatic and beneficial influence on pressure measurements in the first upstream sections, whereas no noticeable effect is observed upon global lift measurements. From the authors' experience, it is highly advisable to arrange a tripping strip at the upstream end of the cylinder when performing such pressure measurements.

Translation

The TLP model predicts no variation of the forces when the cylinder is translated closer to one of its neighbours, refer to (14) with $w \neq 0$ but $w', w'' = 0$. A similar conclusion is obtained by numerical simulations, despite the fact that the velocity in the x–direction is no more uniform (figure 18). In the experiments, a considerable fluid stiffness effect is observed: the lift force is about three times higher in translation than in rotation, in the range of angle and displacement that is investigated here. Thanks to the pressure measurements (figure 20), it is suggested that the stiffness originates from the confinement of the wakes of the supporting rod by the two neighbour cylinders above and below the central cylinder. It is known that end plates with a distance h apart placed on a circular cylinder of diameter D in cross-flow modify the mean base pressure in the near wake. Szepessy and Bearman (1992) have shown that, for aspect ratios $h/D < 1$ and Reynolds numbers $Re_D < 50\,000$, the mean pressure increases as h/D decreases. In the present case, the aspect ratio in neutral configuration is $(P - D)/D_r = 0.7$ and it varies between 0.2 and 1.1 when the cylinder is translated ; the maximum Reynolds number is $Re_{D_r} = 47\,000$. It is then likely that the pressure increases in the smaller gap and decreases in the larger gap produced by the cylinder translation from its initial position, thus introducing the positive fluid stiffness. Therefore, the zero fluid stiffness property of the TLP model is valid only provided that no significant cross-flow body is present. This might seriously limit the applicability of this version of the TLP model to industrial structures.

Bending

Introducing the deformed shape of the cylinder from (2) into the expression of the TLP local forces, (12) and (14), then integrating over the cylinder span yields the following global force

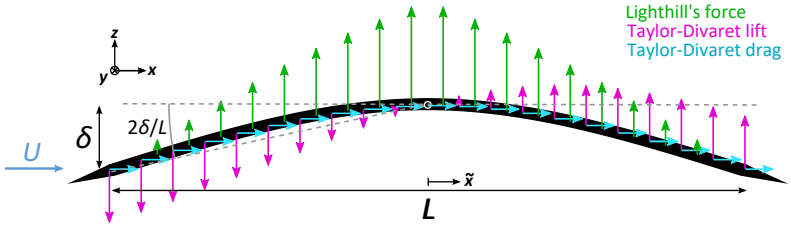

Figure 23: Three terms of the TLP model for a bent cylinder. The same scale is used for both lift forces (with $c_L = 0.10$ and $\chi = 1.38$), another scale is used for the drag.

and moment coefficients:

$$C_L = \chi \frac{3\pi}{2} \frac{2\eta - 1}{\lambda} \frac{D}{L} (2\delta/L),$$
$$C_M = -\left(c_L \frac{8\eta - 3}{16\lambda} + C_D \frac{4\eta - 1}{16\lambda} \right) (2\delta/L), \tag{17}$$

with the parameters $\lambda = 1 + 3l/L = 1.24$ and $\eta = 1 + 2l/L = 1.16$ for the present geometry.

As illustrated in figure 23, the global lift consists of Lighthill's term only (of the three coefficients of the TLP model, only χ appears in the expression of C_L). This term does not contribute to the global pitching moment coefficient C_M. The dominant contribution in C_M is the one from the Taylor-Divaret lift (identified by the coefficient c_L), which is about ten times greater than the contribution of the friction drag (C_D).

While experimental and numerical results agree on the global lift force (figure 21*a*), they do not comply with the predictions of the TLP model, which presents an increased lift with bending. However, excluding the contribution of the tapered ends of the cylinder in CFD restores the expected behaviour from the TLP model. This emphasizes that the local fluid forces at the cylinder ends can have a non-negligible influence on the global force. As for the pitching moment (figure 21*b*), all curves show a behaviour compatible with the TLP model, although with a slightly steeper absolute slope.

As previously mentioned, no pressure measurements could be carried out with a bending cylinder because of design constraints. However, experimental and numerical results agree quite well on the global fluid loadings, so that reliable information on the local forces can be retrieved from CFD. The dashed blue line in figure 22 illustrates the lift distribution along the cylinder according to the TLP model with the coefficients chosen in the introduction of the present section. For the specific case of a statically bent cylinder having an Euler-Bernoulli beam behaviour, the model predicts a steady increase of the lift in the upstream half, a slope discontinuity in the middle and a much flatter evolution in the downstream half. The CFD results agree qualitatively with those three features, though with strong differences in the regions close to the cylinder ends. The green dashed-dotted line shows that the TLP model can be partially fitted to the CFD results with not so drastic updating of its coefficients ($\chi = 1.50$ and $c_L = 0.17$). Actually, the best fit would require a lower value of c_L in the upstream half than in the downstream half. The asymmetric distribution of the viscous contribution to the lift force upon a curved cylinder was also observed numerically by De Ridder et al. (2015).

On the whole, the TLP model is supported by the experimental and numerical investigations undertaken in the present study. Yet it is worth highlighting the fact that, when performing similar experiments as the present ones, special attention must be given to sections of the cylinder that are close to its ends or to supporting elements.

5. Conclusions

In this paper, an extensive experimental and numerical study has been carried out on the steady fluid forces exerted upon a cylinder in axial flow and confined in a cylinder array. The influence of three basic static perturbations (rotation, translation, bending) has been thoroughly investigated. The results have been compared with a semi-empirical model from the literature, identified here as the Taylor-Lighthill-Païdoussis (TLP) model. This model is traditionally used for studying instabilities of slender structures in axial flow, and its governing coefficients are usually fitted on the dynamic behaviour instead of being measured directly. It was found that the model is quite accurate in the case of an ideal axial-flow structure: describing the friction drag as uniform and constant, and the local lift as depending on the local inclination and curvature, seems to give a satisfying picture of the fluid forces, as long as the cylinder section considered is not too close to geometrical singularities. However, in the presence of cross-flow supports, two main features that are not described by the model were identified. In rotation, the local lift force in the wake of the support is much weaker than outside of it. Since the trend remains linear everywhere, the average lift coefficient upon the whole cylinder does exhibit the predicted linear relationship with respect to the angle of inclination, yet the coefficient of proportionality can vary in a not so narrow range. In translation, a considerable fluid stiffness effect was measured and could be qualitatively attributed to specific wake characteristics of cross-flow cylinders at low aspect ratios. These effects should be kept in mind when analysing results on industrial structures in axial flow, where cross-flow elements are most likely to be present.

This study focused on steady forces in the case of static perturbations. In the limit of slow oscillations, it is reasonable to assume that force coefficients identified in steady conditions can be safely used in dynamic conditions. Such an idea can be applied to industrial issues, as in e.g. Moussou et al. (2017).

Declaration of competing interest

The authors declare that they have no known competing financial interests or personal relationships that could have appeared to influence the work reported in this paper.

CRediT authorship contribution statement

Aurélien Joly: Conceptualization, Methodology, Formal analysis, Investigation, Writing - original draft, Project administration. **Nicolas de Buretel de Chassey:** Methodology, Resources. **Alexandre Martin:** Methodology, Software, Writing - review & editing. **Olivier Cadot:** Conceptualization, Writing - original draft. **Luc Pastur:** Conceptualization, Writing - review & editing. **Pierre Moussou:** Conceptualization, Writing - review & editing, Funding acquisition.

Acknowledgements

The authors would like to thank Prof. Olivier Doaré for the fruitful conversations on the TLP model and especially the influence parameters on its coefficients, Mohmad Almoteri for his contribution in the numerical determination of the added mass coefficient, Wen Wen and Sébastien Corre for thoroughly improving the numerical simulations, Jiapeng Ma for his help in performing the pressure measurements, and Pierre Badel for his support, which went far beyond his position of project manager. Mentioning all the staff members of EDF R&D and ENSTA Paris that were involved in this research project would be too long but the authors gratefully acknowledge their input. The authors would also like to thank Prof. Michael P. Païdoussis for kindly encouraging them to publish these results.

References

Adjiman, J., Moussou, P., Doaré, O., Berro, H., Pascan, O., Berland, J., 2016. Divergence modes of a cluster of simply supported arrays in axial flow, in: Proceedings FIV 11.

Archambeau, F., Méchitoua, N., Sakiz, M., 2004. Code_saturne: a finite volume code for the computation of turbulent incompressible flows. International Journal on Finite Volumes 1.

Chen, S., 1975a. Vibration of nuclear fuel bundles. Nuclear Engineering and Design 35, 399–422.

Chen, S., 1975b. Vibrations of a row of circular cylinders in a liquid. Journal of Engineering for Industry 97, 1212–1218.

Chen, S., Wambsganss, M.W., 1972. Parallel-flow-induced vibration of fuel rods. Nuclear Engineering and Design 18, 253–278.

Chung, H., Chen, S., 1977. Vibration of a group of circular cylinders in a confined fluid. Journal of Applied Mechanics 44, 213–217.

De Ridder, J., Degroote, J., Van Tichelen, K., Schuurmans, P., Vierendeels, J., 2013. Modal characteristics of a flexible cylinder in turbulent axial flow from numerical simulations. Journal of Fluids and Structures 43, 110–123.

De Ridder, J., Degroote, J., Van Tichelen, K., Vierendeels, J., 2017. Predicting modal characteristics of a cluster of cylinders in axial flow: From potential flow solutions to coupled CFD–CSM calculations. Journal of Fluids and Structures 74, 90–110.

De Ridder, J., Doaré, O., Degroote, J., Van Tichelen, K., Schuurmans, P., Vierendeels, J., 2015. Simulating the fluid forces and fluid-elastic instabilities of a clamped–clamped cylinder in turbulent axial flow. Journal of Fluids and Structures 55, 139–154.

De Santis, D., Shams, A., 2017. Numerical modeling of flow induced vibration of nuclear fuel rods. Nuclear Engineering and Design 320, 44–56.

Divaret, L., Cadot, O., Moussou, P., Doaré, O., 2014. Normal forces exerted upon a long cylinder oscillating in an axial flow. Journal of Fluid Mechanics 752, 649–669.

Ersdal, S., Faltinsen, O.M., 2006. Normal forces on cylinders in near-axial flow. Journal of Fluids and Structures 22, 1057–1077.

Haaland, S.E., 1983. Simple and explicit formulas for the friction factor in turbulent pipe flow. Journal of Fluids Engineering 105, 89–90.

Hawthorne, W.R., 1961. The early development of the dracone flexible barge. Proceedings of the Institution of Mechanical Engineers 175, 52–83.

Heenan, A.F., Morrison, J.F., 2002. Turbulent boundary layers on axially inclined cylinders. Part 1. Surface-pressure/velocity correlations. Experiments in Fluids 32, 547–557.

ter Hofstede, E., Kottapalli, S., Shams, A., 2017. Numerical prediction of flow induced vibrations in nuclear reactor applications. Nuclear Engineering and Design 319, 81–90.

Joly, A., 2018. Forces fluides stationnaires exercées sur un faisceau de cylindres en écoulement axial et confiné – application au dimensionnement sismique des assemblages combustibles. Ph.D. thesis. Université Paris-Saclay.

de Langre, E., Païdoussis, M.P., Doaré, O., Modarres-Sadeghi, Y., 2007. Flutter of long flexible cylinders in axial flow. Journal of Fluid Mechanics 571, 371–389.

Lighthill, M.J., 1960a. Mathematics and aeronautics. Journal of the Royal Aeronautical Society 64, 375–394.

Lighthill, M.J., 1960b. Note on the swimming of slender fish. Journal of Fluid Mechanics 9, 305–317.

Lopes, J., Païdoussis, M.P., Semler, C., 2002. Linear and nonlinear dynamics of cantilevered cylinders in axial flow. part 2: the equations of motion. Journal of Fluids and Structures 16, 715–737.

Modarres-Sadeghi, Y., Païdoussis, M.P., Semler, C., 2005. A nonlinear model for an extensible slender flexible cylinder subjected to axial flow. Journal of Fluids and Structures 21, 609–627.

Moretti, P.M., Lowery, R.L., 1976. Hydrodynamic inertia coefficients for a tube surrounded by rigid tubes. Journal of Pressure Vessel Technology 98, 190–193.
Moussou, P., Guilloux, A., Boccaccio, E., Ricciardi, G., 2017. Fluid damping in fuel assemblies, in: Proceedings of the ASME 2017 Pressure Vessels and Piping Conference, Waikoloa, HI, USA.
Païdoussis, M.P., 1966a. Dynamics of flexible slender cylinders in axial flow. Part 1: theory. Journal of Fluid Mechanics 26, 717–736.
Païdoussis, M.P., 1966b. Dynamics of flexible slender cylinders in axial flow. Part 2: experiments. Journal of Fluid Mechanics 26, 737–751.
Païdoussis, M.P., 1973. Dynamics of cylindrical structures subjected to axial flow. Journal of Sound and Vibration 29, 365–385.
Païdoussis, M.P., 1979. The dynamics of clusters of flexible cylinders in axial flow: theory and experiments. Journal of Sound and Vibration 65, 391–417.
Païdoussis, M.P., 2016. Fluid-Structure Interactions: Slender Structures and Axial Flow. volume 2. 2 ed., Elsevier Academic Press, London.
Païdoussis, M.P., Grinevich, E., Adamovic, D., Semler, C., 2002. Linear and nonlinear dynamics of cantilevered cylinders in axial flow. part 1: physical dynamics. Journal of Fluids and Structures 16, 691–713.
Païdoussis, M.P., Suss, S., 1977. Stability of a cluster of flexible cylinders in bounded axial flow. Journal of Applied Mechanics 44, 401–408.
Papukchiev, A., Pandazis, P., Hristov, H.V., Scheuerer, M., 2018. Validation of coupled CFD–CSM methods for vibration phenomena in nuclear reactor cores, in: IUTAM symposium on critical flow dynamics around moving/deformable structures with design applications, Santorini, Greece.
Relf, E.F., Powell, C.H., 1917. Tests on smooth and stranded wires inclined to the wind direction, and a comparison of results on stranded wires in air and water. Advisory Committee for Aeronautics, London, R&M 307.
Ricciardi, G., 2018. Parametric study on confinement effect on a fuel assembly dynamical behavior under axial flow. Journal of Fluids and Structures 78, 109–125.
Rinaldi, S., Païdoussis, M.P., 2020. An improved theoretical model for the dynamics of a free–clamped cylinder in axial flow. Journal of Fluids and Structures 94, 102903.
Semler, C., Lopes, J., Augu, N., Païdoussis, M.P., 2002. Linear and nonlinear dynamics of cantilevered cylinders in axial flow. part 3: nonlinear dynamics. Journal of Fluids and Structures 16, 739–759.
Szepessy, S., Bearman, P.W., 1992. Aspect ratio and end plate effects on vortex shedding from a circular cylinder. Journal of Fluid Mechanics 234, 191–217.
Tavoularis, S., 2005. Measurement in Fluid Mechanics. Cambridge University Press, New York.
Taylor, G.I., 1952. Analysis of the swimming of long and narrow animals. Proceedings of the Royal Society of London A: Mathematical, Physical and Engineering Sciences 214, 158–183.
White, F.M., 2011. Fluid Mechanics. 7 ed., McGraw-Hill, New York.